Intensity Based Image Registration By Nonparametric Local Smoothing

Chen Xing and Peihua Qiu

Abstract—Image registration is used widely in applications for mapping one image to another. Existing image registration methods are either feature-based or intensity-based. Feature-based methods first extract relevant image features, and then find a geometrical transformation that best matches the two corresponding sets of features extracted from the two images. Because identification and extraction of image features is often a challenging and time-consuming process, intensity-based image registration, by which the mapping transformation is estimated directly from the observed image intensities of the two images, has received much attention recently. In the literature, most existing intensity-based image registration methods estimate the mapping transformation globally by solving a minimization/maximization problem defined by the two entire images to register. To this end, it needs to be assumed that the mapping transformation has a certain type of parametric form or it is a continuous bivariate function satisfying certain regularity conditions. In this paper, we propose a novel intensity-based image registration method using nonparametric local smoothing. By this method, the mapping transformation at a given pixel is estimated locally in a neighborhood, after certain image features are accommodated in the estimation. Due to the flexibility of local smoothing, this method does not require any parametric form for the mapping transformation. It even allows the transformation to be a discontinuous function. Numerical examples show that it is effective in various applications.

Index Terms—Degeneration, discontinuity, edge detection, local smoothing, mapping, nonparametric transformation, weighted least squares estimation.

1 Introduction

IMAGE registration aims to geometrically match up two or more images of the same scene, taken at different times, from different viewpoints, or by different sensors, for structure/target localization, difference detection, and many other purposes [40]. It is widely used in medical imaging [16], remote sensing [18], finger print or face recognition [19], image compression [8], video enhancement [14], and so forth. In medical imaging, for instance, a common application of this technique is to integrate useful information from different sources (e.g., CT, PET, SPECT, X-ray, ultrasound, and MRI images [20], [22]), or to register images obtained at different times [33]. It has become an important tool for improving the quality of certain image-based technologies [21].

Mathematically, the image registration problem can be described as follows. Let $Z_R(x,y)$ and $Z_M(x,y)$ be a reference image and an image to register with, respectively. Because $Z_M(x,y)$ is usually a geometrically altered version of $Z_R(x,y)$, it is often called a moved image in the literature. Then, the major goal of image registration is to find a geometrical transformation $\mathbf{T}(x,y) = (T_1(x,y), T_2(x,y))$ such that $Z_M(\mathbf{T}(x,y))$ is as close to $Z_R(x,y)$ as possible. Thus, the image registration problem can be formulated as the following maximization problem:

$$\mathbf{T}_{opt} = \arg\max_{\mathbf{T}\in\mathcal{T}} S(Z_R, Z_M(\mathbf{T})), \tag{1}$$

where $\mathbf{T}_{opt}$ denotes the optimal transformation for matching $Z_R(x,y)$ and $Z_M(x,y)$ among all possible transformations in a specific transformation space $\mathcal{T}$, and S is a selected metric for measuring similarity between the two images. In (1), if a dissimilarity metric is used in place of the similarity metric S, then the maximization problem becomes a minimization problem. See [30] for a discussion about image registration in MRI applications, and for a description about various existing similarity/dissimilarity metrics.

In the literature, there are mainly two types of image registration methods. The first type selects a number of corresponding *features* in the two images, respectively, and then finds a geometrical transformation to best match the two sets of features [1], [6]. To this end, landmarks or control points are often the preferred features and they can be selected manually or automatically by a computer [39]. Other commonly used features include edge lines or curves, which are often detected by gradient-based methods, and regions, centroids or templates, which are usually determined by ways of thresholding and segmentation [34]. For comprehensive surveys, see [5], [40]. In some real applications, however, there are some limitations within these feature-based methods. First, feature selection is often a time-consuming and challenging process with much arbitrariness involved. Second, it is often difficult to determine

C. Xing is with the School of Statistics, University of Minnesota, Minneapolis, MN 55455, USA. E-mail: xing@stat.umn.edu.
P. Qiu is with the School of Statistics, University of Minnesota, Minneapolis, MN 55455, USA. E-mail: qiu@stat.umn.edu.

the number of needed features. The more features we select, the higher accuracy we could possibly achieve for estimating the geometrical transformation. But at the same time more effort is required. Several methods have been proposed to select a subset of detected features without sacrificing much of the image registration quality. See, for instance, [11], [17].

Rather than selecting features for image registration, the second type of methods tries to search for a geometrical transformation from a specific transformation space such that Z_R and Z_M best match each other, in terms of a similarity/dissimilarity metric defined directly by the observed image intensities, as described in (1). This type of *intensity-based* image registration (IBIR) procedures is flexible to use, and has become popular in various applications. Most existing IBIR procedures estimate the geometrical transformation $\mathbf{T}$ globally by solving a minimization/maximization problem, such as (1), with the two entire images Z_R and Z_M involved. To this end, we need to assume that $\mathbf{T}$ follows a parametric model or it is a continuous bivariate function satisfying certain regularity conditions [21]. A widely used 2-D parametric transformation is defined by

$$\begin{cases} T_1(x,y) &= \alpha(x\cos\Delta\phi + y\sin\Delta\phi) + \Delta x \\ T_2(x,y) &= \alpha(-x\sin\Delta\phi + y\cos\Delta\phi) + \Delta y, \end{cases} \quad (2)$$

where $(\Delta x, \Delta y, \Delta\phi)$ are three motion parameters and α is a scaling parameter. Model (2) describes rigid-body motions (i.e., distance between any two points on an object is unchanged during the motion) when $\alpha = 1$. It has been commonly used in applications [7] for various reasons, including the ease of implementation and computation, and its feature preservation property (e.g., a line maps to a line). Recently, much research progress has been made to generalize model (2). For instance, free-form deformation (DDF) techniques are getting popular in the image registration community, due to their relatively simple computation and other salient properties [37], [36]. DDF methods approximate the transformation $\mathbf{T}$ using B-splines with knots chosen properly beforehand. Diffeomorphic image registration also attracts much attention recently, by which the transformation $\mathbf{T}$ is determined by solving a differential equation [4], [2]. Other recent methods include those using Fourier transformations [23], [15], and information-theoretical tools [32], [25], among many others. Klein et al. [16] made a comprehensive evaluation of 14 commonly used IBIR algorithms and evaluation criteria using various test images.

In the literature, there are a number of registration methods that try to overcome certain limitations of both the feature-based and the intensity-based methods. See, for instance, [38], [24]. There are also some related research areas. As an example, optical flow techniques are for processing image sequences [13], [3]. Some ideas there might be helpful for image registration, although the two research problems have some substantial differences.

Global estimation methods are efficient when the assumed parametric models or regularity conditions of $\mathbf{T}$ are valid. But, validity of such models or regularity conditions should be justified properly in applications, which would be challenging and is currently lacking. In this paper, we try to tackle the IBIR problem using nonparametric local smoothing. Namely, estimation of $\mathbf{T}$ at a given pixel depends only on nearby image intensities of the two images, instead of on all image intensities of the two images. This *local estimation* nature makes it possible to not impose restrictive assumptions on $\mathbf{T}$. Under this local smoothing framework, a novel IBIR method is proposed, by which the mapping transformation $\mathbf{T}$ at a given pixel is estimated locally in a neighborhood, after certain image features are accommodated in the estimation. This method does not require any parametric form for $\mathbf{T}$. It even allows $\mathbf{T}$ to be a discontinuous function.

The rest part of the article is organized as follows. In Section 2, our proposed IBIR procedure is described in detail. Various numerical experiments and comparisons with some existing methods are presented in Section 3. Certain concluding remarks are given in Section 4.

2 Proposed Method

Our proposed method is described in three parts. After a statistical model for describing the IBIR problem is introduced in Section 2.1, a scheme for classifying pixels is defined in Section 2.2. Then, the proposed IBIR procedure is described in Section 2.3.

2.1 Statistical Model

Description (1) of the image registration problem is commonly used in the medical imaging and computer sciences communities. A statistically more precise description of the problem might be as follows. Let R and M be two images to register. Their true image intensity functions are denoted as $R(x,y)$ and $M(x,y)$. It is assumed that they have the following relationship:

$$M(T_1(x,y), T_2(x,y)) = R(x,y), \text{ for } (x,y) \in \Omega, \quad (3)$$

where Ω is the design space of the image R, and $\mathbf{T}(x,y) = (T_1(x,y), T_2(x,y))$ is an unknown geometrical transformation to estimate. IBIR methods try to estimate $\mathbf{T}(x,y)$ from observed image intensities of the two images defined below.

$$\begin{aligned} Z_M(x_i,y_j) &= M(x_i,y_j) + \varepsilon_M(x_i,y_j), \\ Z_R(x_i,y_j) &= R(x_i,y_j) + \varepsilon_R(x_i,y_j), \\ &\quad \text{for } i,j = 1,2,\ldots,n, \end{aligned} \quad (4)$$

where $\{(x_i,y_j)\}$ are pixel locations, and $\{\varepsilon_M(x_i,y_j)\}$ and $\{\varepsilon_R(x_i,y_j)\}$ are i.i.d. random errors in the two images with mean 0 and unknown variances σ_M^2 and σ_R^2, respectively. Nonparametric intensity-based image registration (NIBIR) tries to estimate $\mathbf{T}(x,y)$ from the observed image intensities, without imposing any parametric form on

$\mathbf{T}(x,y)$. In (4), we assume that the two observed images contain pointwise noise only, for simplicity. In practice, they may also contain spatial blur and other degradations [12], [28]. A numerical example in Section 3 shows that our proposed method also works well when spatial blur is present. At a given point $(x,y) \in \Omega$, we can write

$$\begin{pmatrix} T_1(x,y) \\ T_2(x,y) \end{pmatrix} = \begin{pmatrix} x \\ y \end{pmatrix} + \begin{pmatrix} b(x,y) \\ c(x,y) \end{pmatrix},$$

where $b(x,y) = T_1(x,y) - x$ and $c(x,y) = T_2(x,y) - y$. Therefore, estimation of $\mathbf{T}(x,y)$ is equivalent to estimation of $(b(x,y), c(x,y))$. After the estimators of $(b(x,y), c(x,y))$, denoted as $(\widehat{b}(x,y), \widehat{c}(x,y))$, are obtained, the estimator of $\mathbf{T}(x,y)$ can be written as

$$\widehat{\mathbf{T}}(x,y) = (x,y) + (\widehat{b}(x,y), \widehat{c}(x,y)). \tag{5}$$

2.2 Local Degenerate Pixels

Ideally, if both $b(x,y)$ and $c(x,y)$ are small and M has the first-order partial derivatives at (x,y), then by the Taylor's expansion, we have

$$\begin{aligned} M(T_1(x,y), T_2(x,y)) = M(x,y) + M'_x(x,y)b(x,y) + \\ M'_y(x,y)c(x,y) + o\left(\|\mathbf{T}(x,y) - (x,y)\|\right), \end{aligned} \tag{6}$$

where $\|\cdot\|$ is the Euclidean norm. By (3) and (6), $R(x,y) = M(T_1(x,y), T_2(x,y))$ can be well approximated by $M(x,y) + M'_x(x,y)b(x,y) + M'_y(x,y)c(x,y)$ in such cases. Therefore, $(b(x,y), c(x,y))$ can be chosen such that the approximation error

$$R(x,y) - \left[M(x,y) + M'_x(x,y)b(x,y) + M'_y(x,y)c(x,y)\right]$$

is as small as possible. In reality, however, $R(x,y)$, $M(x,y)$, $M'_x(x,y)$, and $M'_y(x,y)$ are all unobservable. What observed are image intensities $\{Z_M(x_i,y_j)\}$ and $\{Z_R(x_i,y_j)\}$ defined in (4), which contain random noise. To smooth out noise while estimate $(b(x,y), c(x,y))$, we adopt the idea of local linear kernel (LLK) estimation in statistical nonparametric regression [9] as follows. For the time being, let us assume that $M'_x(x,y)$ and $M'_y(x,y)$ have been estimated by $\widehat{M}'_x(x,y)$, and $\widehat{M}'_y(x,y)$ beforehand. Consider a circular neighborhood of (x,y) with radius h_n, denoted as $O(x,y;h_n)$. Then, $b(x,y)$ and $c(x,y)$ can be estimated by the solution of the following minimization problem:

$$\begin{aligned} \min_{b(x,y),c(x,y)} \sum_{i,j=1}^{n} \left[Z_M(x_i,y_j) - Z_R(x_i,y_j) + \right. \\ \left. \widehat{M}'_x(x_i,y_j)b(x,y) + \widehat{M}'_y(x_i,y_j)c(x,y)\right]^2 K_{h_n}, \end{aligned} \tag{7}$$

where $K_{h_n} = K(\frac{x_i - x}{h_n}, \frac{y_j - y}{h_n})$, and K is a bivariate density kernel function with unit circular support. The minimization problem (7) searches for estimators of $b(x,y)$ and $c(x,y)$ such that the weighted sum of squares of the approximation error reaches the minimum, and the weights are determined by the kernel function K. Usually, $K(u,v)$ is chosen to be a decreasing function of $\sqrt{u^2+v^2}$. Therefore, if a pixel $(x_i,y_j) \in O(x,y;h_n)$ is farther away from the given pixel (x,y), then the corresponding approximation error at (x_i,y_j) would receive a less weight, which is intuitively reasonable, because the observed image intensity at (x_i,y_j) generally provides less information about $(b(x,y), c(x,y))$, compared to observed image intensities at pixels closer to (x,y). In the statistical literature (cf., Section 2.3 in [27]), there exists much discussion about selection of the kernel function K. Commonly used kernel functions include the Epanechnikov kernel function and the truncated Gaussian kernel function that is used in Section 3. It is not difficult to check that problem (7) has the following solution

$$\begin{pmatrix} \widehat{b}(x,y) \\ \widehat{c}(x,y) \end{pmatrix} = \frac{\begin{pmatrix} K_{22}, & -K_{12} \\ -K_{12}, & K_{11} \end{pmatrix} \begin{pmatrix} K_1^* \\ K_2^* \end{pmatrix}}{K_{11}K_{22} - K_{12}^2}, \tag{8}$$

where

$$\begin{aligned} K_{11} &= \sum_{i,j=1}^{n} \left[\widehat{M}'_x(x_i,y_j)\right]^2 K_{h_n}, \\ K_{22} &= \sum_{i,j=1}^{n} \left[\widehat{M}'_y(x_i,y_j)\right]^2 K_{h_n}, \\ K_{12} &= \sum_{i,j=1}^{n} \widehat{M}'_x(x_i,y_j)\widehat{M}'_y(x_i,y_j) K_{h_n}, \\ K_1^* &= \sum_{i,j=1}^{n} \left[Z_R(x_i,y_j) - Z_M(x_i,y_j)\right] \widehat{M}'_x(x_i,y_j) K_{h_n}, \\ K_2^* &= \sum_{i,j=1}^{n} \left[Z_R(x_i,y_j) - Z_M(x_i,y_j)\right] \widehat{M}'_y(x_i,y_j) K_{h_n}. \end{aligned}$$

In practice, we still need to define the estimators $\widehat{M}'_x(x,y)$ and $\widehat{M}'_y(x,y)$. To this end, we suggest using the conventional LLK estimators of $M'_x(x,y)$ and $M'_y(x,y)$, defined by

$$\begin{aligned} \widehat{M}'_x(x,y) &= \frac{\sum_{i,j=1}^{n}(x_i - x)Z_M(x_i,y_j)K_{h_n}}{\sum_{i,j=1}^{n}(x_i - x)^2 K_{h_n}}, \\ \widehat{M}'_y(x,y) &= \frac{\sum_{i,j=1}^{n}(y_j - y)Z_M(x_i,y_j)K_{h_n}}{\sum_{i,j=1}^{n}(y_j - y)^2 K_{h_n}}. \end{aligned}$$

From the above description, we know that formula (8) is obtained in the ideal situation when

(i) $\|\mathbf{T}(x,y) - (x,y)\|$ is small such that the first-order approximation to $M(T_1(x,y), T_2(x,y))$ by (6) is valid,
(ii) M has the first-order partial derivatives at (x,y), and
(iii) the denominator on the right-hand-side of (8) is not zero.

The above conditions (i) and (ii) imply that the estimator defined by (5) and (8) may not estimate $\mathbf{T}(x,y)$ well at places where the transformation is relatively large or where M is not smooth (e.g., edge locations of M). Condition (iii) implies that the estimator is not well

defined at places where the following equation holds:

$$K_{11}K_{22} - K_{12}^2 = 0. \tag{9}$$

Mathematically, it can be proved that: (i) $\widehat{M}'_x(x,y)$ and $\widehat{M}'_y(x,y)$ would converge to $M'_x(x,y)$ and $M'_y(x,y)$, respectively, in regions where M has continuous first-order derivatives, when n gets larger and larger, and (ii) if $\widehat{M}'_x(x,y)$ and $\widehat{M}'_y(x,y)$ are replaced by $M'_x(x,y)$ and $M'_y(x,y)$ in (9), then M satisfies equation (9) in the neighborhood $O(x,y;h_n)$ if and only if there is a continuously differentiable univariate function ψ and a constant ρ such that

$$M(x',y') = \psi(\rho x' + y'), \text{ for any } (x',y') \in O(x,y;h_n). \tag{10}$$

Intuitively, if M satisfies (10) in $O(x,y;h_n)$, then its intensity levels are the same on the line segment $\rho x' + y' = \rho_0$ in $O(x,y;h_n)$, for any appropriate constant ρ_0 such that the line segment is contained in $O(x,y;h_n)$. In such cases, the bivariate function M is degenerate locally in $O(x,y;h_n)$, and it is impossible to uniquely determine $\mathbf{T}(x,y)$ because any small move along the line direction would not change the value of $M(x',y')$ for any $(x',y') \in O(x,y;h_n)$. In this paper, a pixel $(x,y) \in \Omega$ is called a *local degenerate pixel* of M if M has partial derivatives at (x,y) and there exists a neighborhood $O(x,y;h_n)$ such that equation (10) holds. Other pixels at which M has partial derivatives are called *local non-degenerate pixels*. Similarly, we can define local degenerate pixels and local non-degenerate pixels for the reference image R. Therefore, around local degenerate pixels, the image registration problem is actually not well defined in the sense that the geometrical transformation $\mathbf{T}(x,y)$ can not be uniquely determined.

2.3 Proposed Image Registration Procedure

From the description in Section 2.2, it can be seen that the geometrical transformation $\mathbf{T}(x,y)$ can be properly estimated only around local non-degenerate pixels or places where the image intensity function of the reference image R is not smooth. Based on that result, we propose an IBIR procedure consisting of four major steps, as described below.

Step 1 Detect edge pixels for the observed reference image Z_R using an edge detector. see Chapter 6 in [27] for a discussion about existing edge detectors.

Step 2 At a given pixel (x,y) in R, consider its circular neighborhood with radius r_1, denoted as $O(x,y;r_1)$. If the number of detected edge pixels in $O(x,y;r_1)$ is smaller than $[nr_1]$, where $[s]$ denotes the integer part of s, then (x,y) is regarded as a continuity pixel of R. In such a case, if the denominator on the right-hand-side of equation (8) (after M is replaced by R) is larger than or equal to a pre-specified threshold value u_n, then (x,y) is regarded as a local non-degenerate pixel of R; otherwise, it is regarded as a local degenerate pixel.

Step 3 Let $\mathcal{D}$ be the set of all local non-degenerate pixels of R or pixels whose circular neighborhoods with radius r_1 contain at least $[nr_1]$ detected edge pixels. Then, for any $(x,y) \in \mathcal{D}$, $\widehat{\mathbf{T}}(x,y)$ is computed by the following algorithm. For any pixel $(x',y') \in O(x,y;r_1)$ of the moved image, consider its circular neighborhood $O(x',y';r_2)$, where r_2 is a radius that could be different from r_1. Compute the mean squared difference (MSD)

$$MSD((x',y');(x,y)) = \frac{1}{\widetilde{N}} \sum_{(x'+s,y'+t)\in O(x',y';r_2)} \left[Z_M(x'+s,y'+t) - Z_R(x+s,y+t)\right]^2,$$

where $\widetilde{N}$ is the number of pixels in $O(x',y';r_2)$. Then, $\widehat{\mathbf{T}}(x,y)$ is defined to be the minimizer of

$$\min_{(x',y')\in O(x,y;r_1)} MSD((x',y');(x,y)).$$

See Figure 1 for a demonstration.

Step 4 If (x,y) is a local degenerate point of R, then $\widehat{\mathbf{T}}(x,y)$ is defined as follows. First, find a pixel in $\mathcal{D}$ that is closest to (x,y), which is denoted as $(x^{(1)},y^{(1)})$. Then, define

$$\widehat{\mathbf{T}}_1(x,y) = (x,y) + (\widehat{b}(x^{(1)},y^{(1)}), \widehat{c}(x^{(1)},y^{(1)})).$$

Define $\widehat{\mathbf{T}}(x,y) = \widehat{\mathbf{T}}_1(x,y)$ if

$$MSD(\widehat{\mathbf{T}}_1(x,y);(x,y)) \le MSD((x,y);(x,y));$$

otherwise, define $\widehat{\mathbf{T}}(x,y) = (x,y)$.

Note that the above IBIR procedure can only properly handle interior pixels in Ω whose Euclidean distances from the border of Ω are at least $r_1 + r_2$. For a boundary pixel of Ω whose Euclidean distance from the border of Ω is smaller than $r_1 + r_2$, we define the geometrical transformation at that pixel to be the same as that at the interior pixel who is closest to the boundary pixel.

At the end of this section, we make several remarks about the above image registration procedure. First, at local non-degenerate pixels of R, instead of using formulas (5) and (8), we use the searching algorithm described in Step 3 for computing $\widehat{\mathbf{T}}(x,y)$. That is because formula (8) is valid only when $\|\mathbf{T}(x,y) - (x,y)\|$ is small. From our numerical studies, the estimator by the searching algorithm would perform better than the one by (5) and (8) for most realistic $\mathbf{T}(x,y)$ functions. Second, from the discussion in Section 2.2, it seems that, to define $\mathbf{T}(x,y)$ properly, (x,y) should be a non-degenerate pixel of M, instead of R. Again, this discussion is based on the assumption that $\|\mathbf{T}(x,y) - (x,y)\|$ is small so that the Taylor's expansion is valid. In practice, it is more reasonable to require (x,y) to be a non-degenerate pixel of R. Third, in step 3, MSD is used as the matching criterion. Actually, other criteria, including the cross-correlation and entropy of image difference (cf., their definitions in Section 3), can also be considered here. Fourth, computation involved in the searching algorithm described in Step 3 is actually not very extensive because pixels in $\mathcal{D}$ represent only about 10% of all pixels for a typical image.

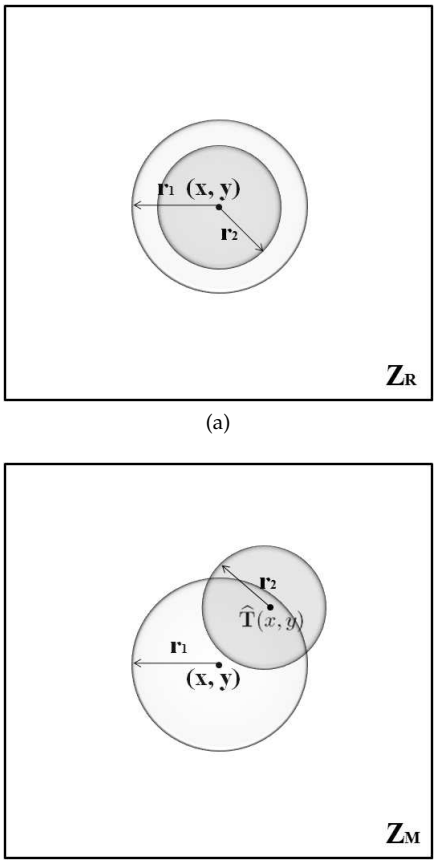

Fig. 1: A demonstration of Step 3 of the proposed image registration algorithm.

3 Numerical Study

We have performed numerical studies with more than 20 different pairs of test images. Here, four representative ones are presented to evaluate the numerical performance of the proposed IBIR procedure. The evaluation is made in comparison with the following two state-of-the-art IBIR methods: the directly manipulated free-form deformation (DMFFD) method [37] and the symmetric diffeomorphic image normalization (SyN) method [2]. Results of both methods depend on the similarity metric that they use. As suggested in the related papers, three similarity metrics, including MSD, cross-correlation (CC), and mutual information (MI), are used respectively in the DMFFD method, and two similarity metrics, including CC and the pure cross correlation (PCC), are used respectively in the SyN method. Therefore, there are total five existing procedures considered here, which are denoted as DMFFD-MSD, DMFFD-CC, DMFFD-MI, SyN-CC, and SyN-PCC. These existing procedures are implemented using the release 1.9 of the software package ANTS that is available at http://www.picsl.upenn.edu/ANTS/. Our proposed nonparametric IBIR procedure is denoted as NEW.

To evaluate the numerical performance of all six procedures, we use three popular measures, including the root residual mean squares (RRMS), the cross correlation (CC), and the entropy of image difference (EID). RRMS is the conventional and most widely used measure. When evaluating an estimator $\widehat{\mathbf{T}}$ of the geometrical transformation $\mathbf{T}$, it is defined to be

$$\text{RRMS} = \left\{ \frac{1}{n^2} \sum_{i,j=1}^{n} \left[Z_R(x_i, y_j) - Z_M(\widehat{\mathbf{T}}(x_i, y_j)) \right]^2 \right\}^{1/2}.$$

Basically, RRMS is the Euclidean distance between $\{Z_R(x_i, y_j)\}$ and $\{Z_M(\widehat{\mathbf{T}}(x_i, y_j))\}$. Therefore, if its value is smaller, then the registration is regarded better. The CC measure is defined to be the Pearson's sample correlation coefficient of the bivariate data $\{(Z_R(x_i, y_j), Z_M(\widehat{\mathbf{T}}(x_i, y_j)))\}$. Intuitively, if the estimator $\widehat{\mathbf{T}}$ is good, then $Z_M(\widehat{\mathbf{T}}(x, y))$ would be close to $Z_R(x, y)$. Consequently, the CC measure would be close to its maximum value 1. So, by this measure, the registration is better if the CC value is larger, although this measure cannot reflect possible scale difference between $Z_R(x, y)$ and $Z_M(\widehat{\mathbf{T}}(x, y))$. The EID measure becomes popular recently [20], [26], [10]. It is defined by

$$\text{EID} = -\sum_{d \in D} p(d) \log p(d),$$

where

$$D = \{Z_R(x_i, y_j) - Z_M(\widehat{\mathbf{T}}(x_i, y_j)),\ i, j = 1, 2, \ldots, n\}.$$

So, EID is basically the negative entropy of D. Intuitively, if $\widehat{\mathbf{T}}$ is a good estimator of $\mathbf{T}$, then the randomness in the elements of D should be large. Consequently, EID should be small because the entropy $\sum_{d \in D} p(d) \log p(d)$ is a good measure of the randomness of D. Therefore, by this measure, the registration is better if the EID value is smaller.

In procedure NEW, the kernel function $K(u, v)$ is chosen to be the truncated bivariate Gaussian density function with support $\{(u, v) : u^2 + v^2 \leq 1\}$. For edge detection, we use the directional derivative along the estimated gradient at a given pixel as an edge detection criterion, and the given pixel is flagged as an edge pixel if the absolute value of the directional derivative exceeds a threshold value. This edge detector is similar to the ones in [29] and [31], and performs reasonably well. We also tried several other edge detectors, including Sobel, LoG, and the recent one in [35], and found that the registration results of the procedure NEW do not change much with different edge detectors. For all six procedures considered, we try all possible values of their procedure parameters and use the ones resulting in the smallest RRMS values.

In the first example shown in Figure 2, the reference image in plot (a) contains mainly a railway and a ball, and the upper half of the reference image is moved to the right in the moved image shown in plot (b). To better demonstrate the move, one specific spot at the railway that looks like a joint and another dark spot

on the ground that is below the railway have been highlighted. It can be seen that both highlighted spots do not change in the two images. Therefore, in this example, the true geometrical transformation $\mathbf{T}$ takes non-zero values in the upper half of the reference image only, and it is thus a discontinuous transformation. The detected edge points and local non-degenerate points of the reference image, detected by our algorithm, are presented in Figure 3, which seem to capture the major image structure well. The restored reference image of

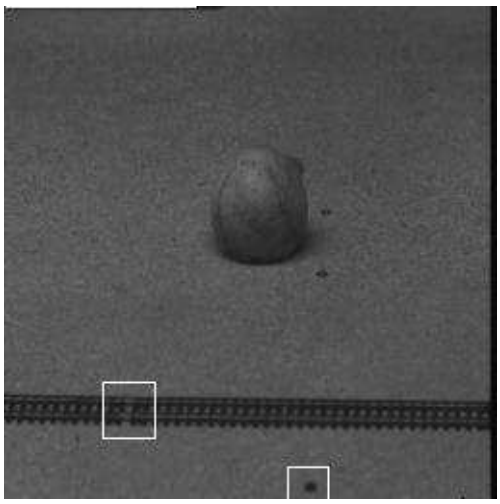

(a)

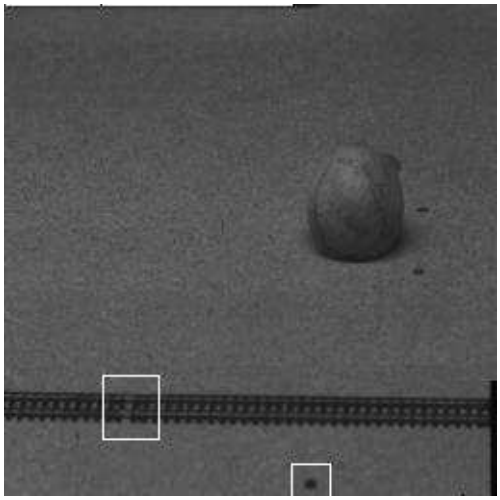

(b)

Fig. 2: (a) A reference image containing a railway and a ball. (b) A corresponding moved image. The two specific spots highlighted in image (a) by the white boxes correspond to those highlighted in image (b).

a given procedure is defined to be $Z_M(\widehat{\mathbf{T}}(x,y))$. Figure 4(a)-(f) show the restored reference images of the six registration procedures, respectively. From the plots, it can be seen that our proposed procedure NEW restores the original position of the ball well. As a comparison, all the five competing procedures seem to move the entire moved image, including the ball, the railway, and the background, to the left, which is evidenced by

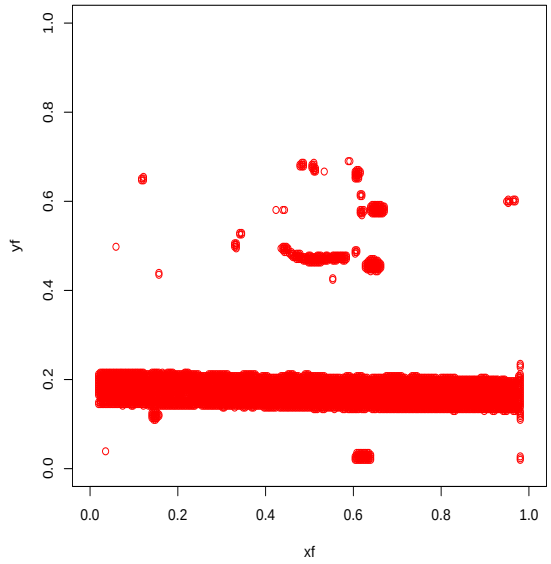

Fig. 3: Detected edge pixels and local non-degenerate pixels of the reference image in the railway-ball example.

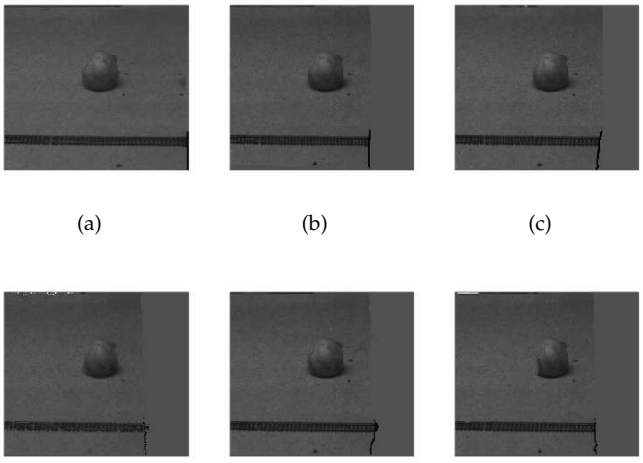

(a) (b) (c)

(d) (e) (f)

Fig. 4: (a)-(f) Restored reference images by procedures NEW, DMFFD-MSD, DMFFD-CC, DMFFD-MI, SyN-CC, and SyN-PCC, respectively, in the railway-ball example.

the positions of the two spots that are highlighted in Figure 2. Consequently, the original position of the ball is restored properly by them. But, the bottom half of the image is improperly moved as well. Our explanation of these results is that all five competing procedures cannot handle cases when $\mathbf{T}(x,y)$ is discontinuous, while our proposed procedure has the flexibility to allow $\mathbf{T}(x,y)$ to be discontinuous, due to the fact that it defines $\widehat{\mathbf{T}}(x,y)$ locally. To further investigate this, the residual images of the six procedures are presented in Figure 5(a)-(f). For a given procedure, the residual image is defined to be $Z_M(\widehat{\mathbf{T}}(x,y)) - Z_R(x,y)$. From the plots, it can be seen that the residual image of the procedure NEW is

TABLE 1: Performance measures of the six procedures in the railway-ball example.

	NEW	DMFFD-MSD	DMFFD-CC	DMFFD-MI	SyN-CC	SyN-PCC
RRMS	10.929	12.760	12.917	13.238	11.945	12.650
CC	0.745	0.641	0.629	0.605	0.699	0.660
EID	2.911	3.101	2.737	3.243	2.845	3.045

almost empty, while the residual images of the other five procedures all show part of the railway clearly, which is consistent with the images shown in Figure 4. The performance measures of the six procedures are presented in Table 1. From the table, it can be seen that procedure NEW is better than all five competing procedures in terms of RRMS and CC. It is better than procedures DMFFD-MSD, DMFFD-MI and SyN-PCC in terms of EID. When reading the table, readers are reminded that the performance of a denoising procedure is better if the RRMS or EID value is smaller or the CC value is larger.

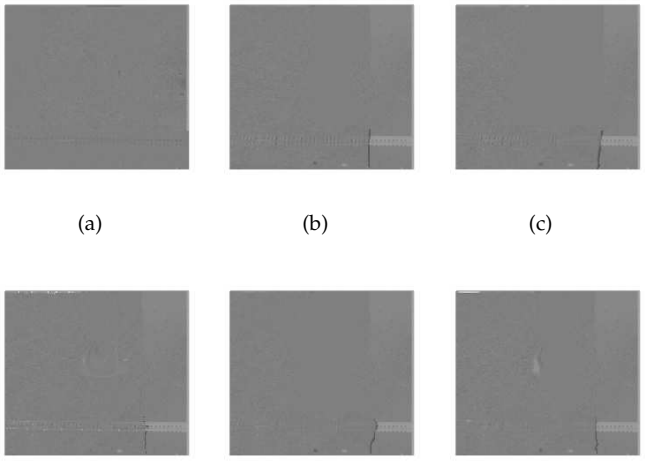

(a) (b) (c)

(d) (e) (f)

Fig. 5: (a)-(f) Residual images of procedures NEW, DMFFD-MSD, DMFFD-CC, DMFFD-MI, SyN-CC, and SyN-PCC, respectively, in the railway-ball example.

(a) (b)

Fig. 6: (a) A reference image containing a bird. (b) A corresponding moved image.

The second example involves a pair of test images shown in Figure 6. The reference image shown in plot (a) contains a bird, and it is twisted in the middle by a continuous transformation resulting in the moved image shown in plot (b). So, in this example, the geometrical transformation $\mathbf{T}$ is a continuous transformation that takes non-zero values in the middle part of the moved image only.

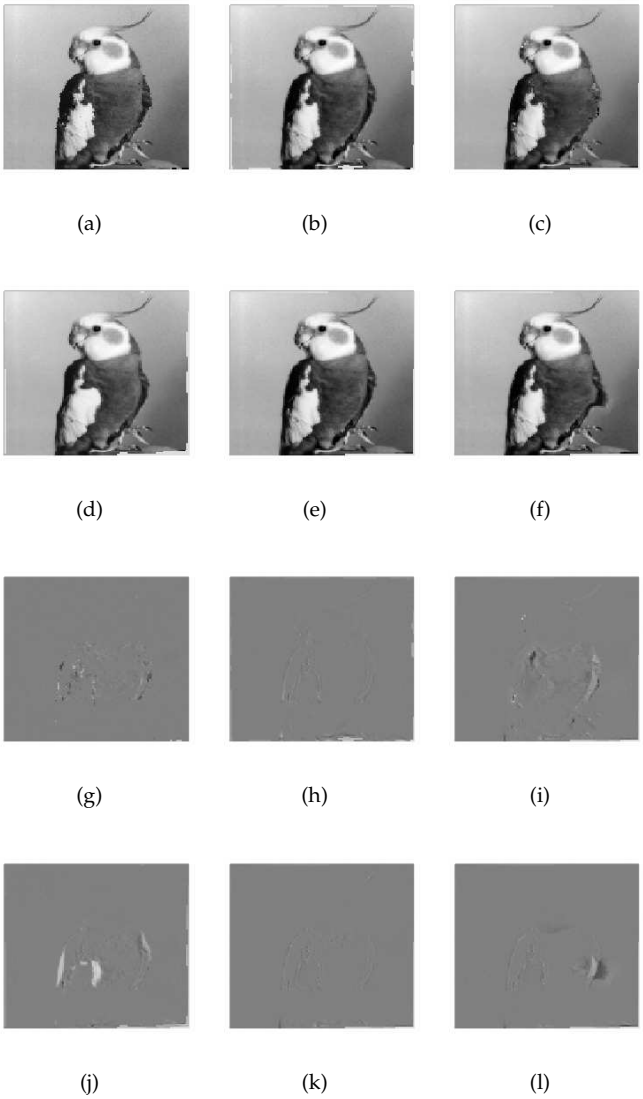

(a) (b) (c)

(d) (e) (f)

(g) (h) (i)

(j) (k) (l)

Fig. 7: (a)-(f) Restored reference images by procedures NEW, DMFFD-MSD, DMFFD-CC, DMFFD-MI, SyN-CC, and SyN-PCC, respectively, in the bird example. (g)-(l) Corresponding residual images of the procedures.

Figure 7(a)-(f) show the restored images of the six procedures. The corresponding residual images of the six procedures are presented in Figure 7(g)-(l), respectively.

TABLE 2: Performance measures of the six procedures in the bird example.

	NEW	DMFFD-MSD	DMFFD-CC	DMFFD-MI	SyN-CC	SyN-PCC
RRMS	7.434	9.333	12.914	18.507	10.401	12.430
CC	0.987	0.980	0.960	0.920	0.975	0.963
EID	1.829	1.801	2.342	2.373	1.680	1.655

From the plots, it seems that procedures NEW, DMFFD-MSD and SyN-CC properly move the bird back to its original position in the reference image. The other three procedures cannot restore part of the altered portion of the bird well (cf., plots (i), (j) and (l)). If we check the plots carefully, then we will find that the five competing procedures do not do well in certain border regions (cf., the left border of plot (b)). The border regions of the reference image are actually unchanged by the true transformation $\mathbf{T}$ in this example. But, some of them are moved by the five competing procedures. By comparing plots (a) and (b), we can also find that the boundary curve of the bird (cf., the left part) is rougher in plot (a), compared to the curve in plot (b). That is the side effect to use a local smoothing method, such as the proposed procedure NEW. Generally speaking, a local smoothing method is more flexible than a global smoothing method, in the sense that it can accommodate discontinuities and other singularities in the transformation $\mathbf{T}(x, y)$, etc.; but, at the same time, the boundary curves of image objects in its restored image would not be as smooth as those in the restored image of the global smoothing method. The RRMS, CC, and EID values of the six procedures are given in Table 2. From the table, we can see that the RRMS value of the procedure NEW is smaller than the corresponding values of the other five procedures in quite large margins in this example. Its CC value is the largest among the CC values of the six procedures. Its EID values are smaller than those of the procedures DMFFD-CC and DMFFD-MI, but larger than those of the procedures DMFFD-MSD, SyN-CC and SyN-PCC.

The next example considers a pair of satellite sensor images taken at the San Francisco bay area. The first one was taken in 1990 and the second one was taken in 1999. By comparing the two images, we can investigate the changes at the San Francisco bay area during the 9-year period. The two images are shown in Figure 8(a)-(b), and they can be downloaded from http://webmodis.iis.u-tokyo.ac.jp/Landsat/. To highlight the difference between the two images, two boxes of different sizes are used in each image to label two specific regions that changed quite a lot during the 9-year period. For instance, in the region labeled by the larger box, there are many more dark pixels in the 1999-image, compared to the 1990-image, which may imply environmental worsening in that region over the 9-year period.

Figure 9(a)-(f) show the restored images of the six registration procedures, and Figure 9(g)-(l) show their residual images in the satellite image example. Performance measures of the related procedures are presented

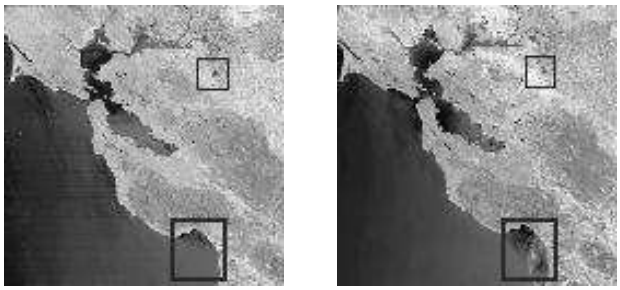

(a) (b)

Fig. 8: (a) A reference satellite image taken in 1990 at the San Francisco bay area. (b) A corresponding satellite image taken in 1999 in the same area. The two dark boxes in each image highlight two specific regions that changed quite a lot during the 9-year period.

in Table 3. From both the residual images and Table 3, it can be seen that our proposed procedure NEW is compatible with its peers in this example. By comparing the residual images (e.g., comparing plot (g) with plot (k)), we can see that the five competing procedures do not perform well at the upper boundary region, which might be one major reason why their performance measures in Table 3 are worse than those of the procedure NEW.

Next we consider a pair of MRI brain images shown in Figure 10(a)-(b). The reference image is downloaded from http://overcode.yak.net/15/. The only difference between the two images is that the dark region around the central part of the reference image is moved upward and rotated in the moved image. Therefore, in this example, the geometrical transformation $\mathbf{T}$ is discontinuous, it takes non-zero values in a small portion of the reference image only.

The restored MRI images and the corresponding residual images of the six procedures are shown in Figure 11(a)-(f) and Figure 11(g)-(l), respectively. From the presented images, we can see that only procedures NEW and SyN-CC register the moved portions of the images well. The moved dark region can be clearly seen in the residual images of procedures DMFFD-MSD, DMFFD-CC, DMFFD-MI, and SyN-PCC, it can be vaguely seen in the residual image of the procedure SyN-CC, and the residual image of the proposed procedure NEW contain the least information about the brain. The RRMS, CC and EID values of the six procedures are presented in Table 4. We can see that procedure NEW has significantly smaller RRMS and EID values than the other five procedures, and its CC value is the largest among all procedures. This

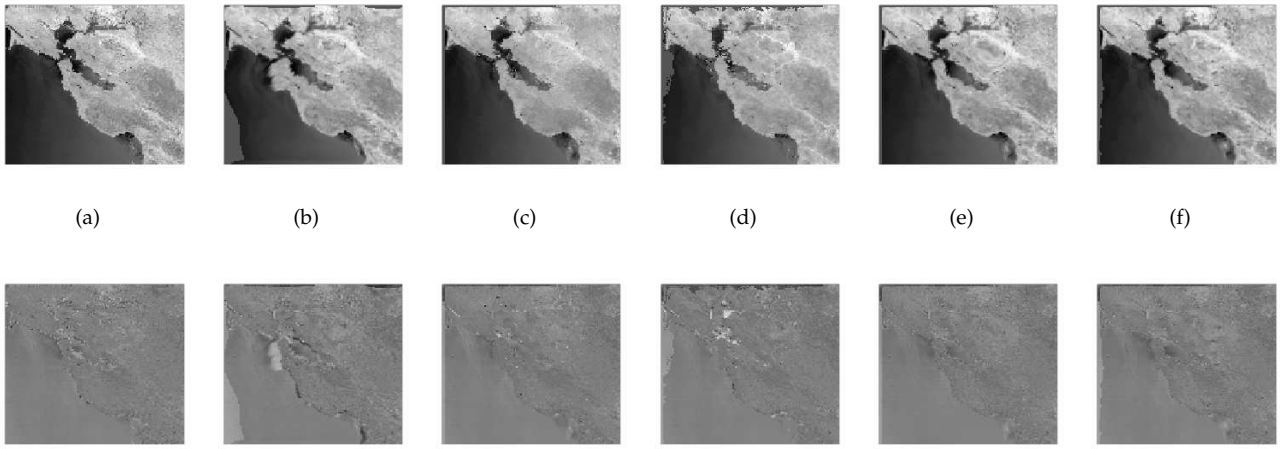

(a) (b) (c) (d) (e) (f)

(g) (h) (i) (j) (k) (l)

Fig. 9: (a)-(f) Restored reference images of procedures NEW, DMFFD-MSD, DMFFD-CC, DMFFD-MI, SyN-CC, and SyN-PCC, respectively, in the satellite image example. (g)-(l) Corresponding residual images of the same procedures.

TABLE 3: Performance measures of the six procedures in the satellite image example.

	NEW	DMFFD-MSD	DMFFD-CC	DMFFD-MI	SyN-CC	SyN-PCC
RRMS	18.782	26.560	20.206	24.980	20.162	21.099
CC	0.951	0.896	0.941	0.908	0.942	0.937
EID	4.143	4.434	4.192	4.196	4.242	4.310

TABLE 4: Performance measures of the six procedures in the MRI example.

	NEW	DMFFD-MSD	DMFFD-CC	DMFFD-MI	SyN-CC	SyN-PCC
RRMS	2.976	9.585	9.459	9.367	4.059	8.838
CC	0.999	0.985	0.986	0.986	0.997	0.987
EID	0.120	0.773	0.484	0.785	0.652	0.460

table also shows that the RRMS and EID values of the procedures SyN-CC and SyN-PCC are quite different, but their CC values are quite close. That can be explained by the fact that CC (or PCC) is used in SyN-CC and SyN-PCC as the similarity metric, causing their CC values close to each other. But, other performance metrics could be different.

In practice, observed images are often blurred [12], [28]. To investigate the performance of the related image registration procedures for matching blurred images, next we consider the pair of blurred images shown in Figure 12(a)-(b), which are blurred versions of the ones shown in Figure 10(a)-(b). In this example, the image intensity functions would be smoother than the ones in the previous example. The restored images and the corresponding residual images of the six procedures are shown in Figure 13, from which it can be seen that the performance of the five competing procedures seems improved in this example, especially for procedures DMFFD-CC and SyN-CC, compared to their performance in the previous example. The RRMS, CC and EID values of the six procedures are presented in Table 5. From the table, we can see that procedure NEW still performs the best in this example in terms of all three measures.

In all the numerical examples considered above, except the railway-ball example, each image has 128×128 pixels. The two images in the railway-ball example have 256×256 pixels each. It takes about 10 seconds for the proposed procedure NEW to register two 128×128 images on a PC of Intel(R) 2.40GHz Core(TM)2 Duo CPU with 2982 MByte memory. Its computational complexity is $O(n^6 r_1^2 r_2^2)$, where r_1 and r_2 are two radii used (cf., Figure 1).

4 Conclusions

In this paper, we propose an intensity-based image registration method which allows the geometrical transformation $\mathbf{T}(x, y) = (T_1(x, y), T_2(x, y))$ to be nonparametric. From the numerical examples shown in Section 3, we can see that this method allows $\mathbf{T}(x, y)$ to be discontinuous in the design space. We also defined local degenerate pixels, around which $\mathbf{T}(x, y)$ cannot be properly defined, which is the ill-posed nature of the IBIR problem. In

TABLE 5: Performance measures of the six procedures in the blurred MRI example.

	NEW	DMFFD-MSD	DMFFD-CC	DMFFD-MI	SyN-CC	SyN-PCC
RRMS	1.814	8.789	2.953	8.015	2.021	7.976
CC	0.999	0.986	0.998	0.989	0.999	0.989
EID	0.164	0.629	0.599	0.429	0.357	0.468

(a)

(b)

Fig. 10: (a) A reference MRI image. (b) A corresponding moved image. The only difference between the two images is that the dark region around the central part of the reference image is moved upward and rotated in the moved image.

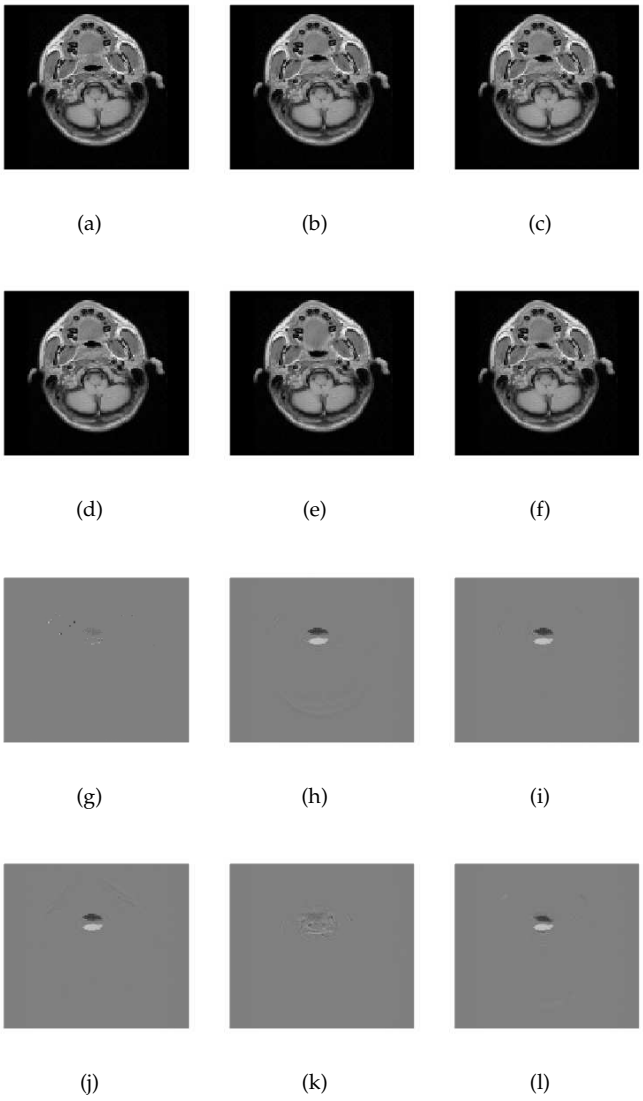

(a) (b) (c)

(d) (e) (f)

(g) (h) (i)

(j) (k) (l)

Fig. 11: (a)-(f) Restored reference images of procedures NEW, DMFFD-MSD, DMFFD-CC, DMFFD-MI, SyN-CC, and SyN-PCC, respectively, in the MRI example. (g)-(l) Corresponding residual images of the same procedures.

the literature, most people do not discuss this ill-posed nature explicitly. Instead, the transformation $\mathbf{T}(x, y)$ is estimated globally in the entire design space, after the ill-posed nature is overcome by imposing a parametric form or other regularization conditions on $\mathbf{T}(x, y)$ [21]. Comparing our proposed local smoothing method with those existing regularization-based global smoothing methods, numerical results in Section 3 show that our method preserves certain local features of $\mathbf{T}(x, y)$ (e.g., discontinuities) better, while the image objects in the restored images of some global smoothing methods might look smoother (cf., related discussion about Figure 7 in Section 3).

In the proposed method, there are still some issues that need to be addressed in our future research. For instance, in the proposed method, there are several parameters, including h_n, u_n, r_1, and r_2. Appropriate selection of these

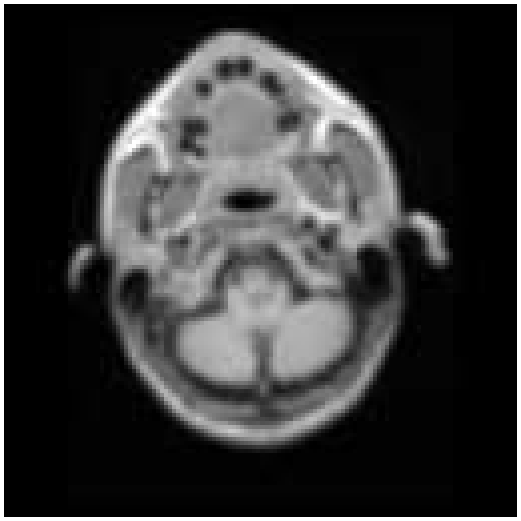

(a)

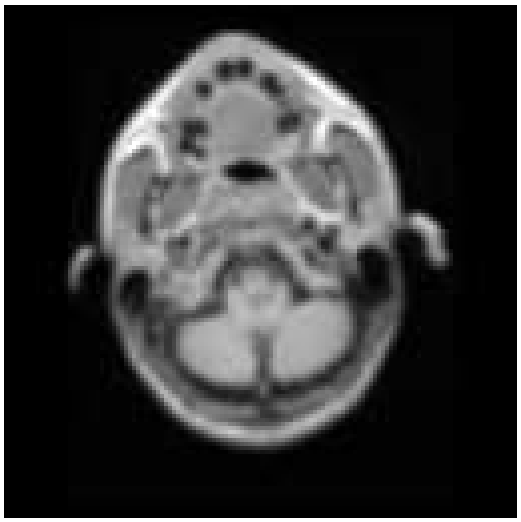

(b)

Fig. 12: (a) A reference MRI image. (b) A corresponding moved image. They are blurred versions of the ones shown in Figure 10.

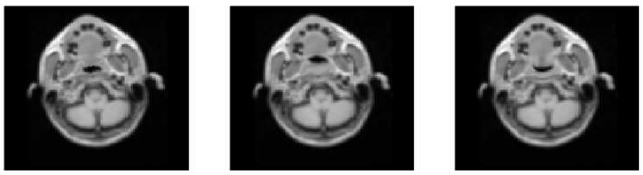

(a) (b) (c)

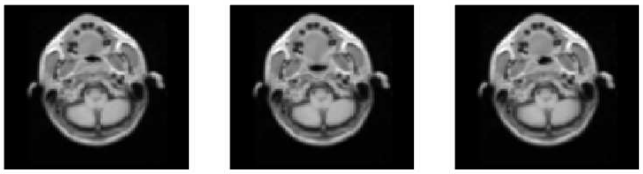

(d) (e) (f)

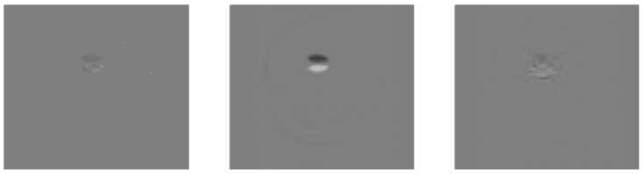

(g) (h) (i)

(j) (k) (l)

Fig. 13: (a)-(f) Restored reference images of procedures NEW, DMFFD-MSD, DMFFD-CC, DMFFD-MI, SyN-CC, and SyN-PCC, respectively, in the blurred MRI example. (g)-(l) Corresponding residual images of the same procedures.

parameters based on observed images is an important topic, which has not been properly addressed yet. To this end, cross-validation, generalized cross-validation, bootstrap and other parameter selection methods discussed in the statistical literature (e.g., Sections 2.4 and 2.5 in [27]) might be helpful. In our numerical study, we have used the 2-D truncated Gaussian density function as the kernel used by the local smoothing procedure (7). It requires much future research to study whether other kernel functions would generate a better image registration. The magnitude of $\mathbf{T}(x, y)$ is also an important factor that affects the performance of all registration procedures considered in section 3. Based on our numerical experience, the proposed procedure NEW would perform well when $\max_{(x,y)\in\Omega} \|\mathbf{T}(x, y) - (x, y)\| \leq 0.25$, if the design space of an entire image is considered to be $[0, 1] \times [0, 1]$. When the magnitude of $\mathbf{T}(x, y)$ is large, maybe we should find a global parametric transformation first to account for global trend of the geometrical transformation and then apply the local registration procedure suggested here to accommodate certain local features of the transformation, which will be further investigated in our future research.

5 Acknowledgments

This research is supported in part by an NSF grant. The authors thank Dr. Nick Tustison for helpful conversations regarding the implementation of the software package ANTS. The editor and four referees provided many constructive comments and suggestions, which greatly improved the quality of the paper.

REFERENCES

[1] R. J. Althof, M. G. J. Wind, and J. T. Dobbins. A rapid and automatic image registration algorithm with subpixel accuracy. *IEEE Transactions on Medical Imaging*, 16:308–316, 1997.

[2] B. Avants, C. Epstein, M. Grossman, and J. Gee. Symmetric diffeomorphic image registration with cross-correlation: Evaluating automated labeling of elderly and neurodegenerative brain. *Medical Image Analysis*, 12:26–41, 2008.

[3] J. Barron, D. Fleet, and S. Beauchemin. Performance of optical flow techniques. *International Journal of Computer Vision*, 12(1):43–77, 1994.

[4] F. Beg, M. Miller, A. Trouv'e, and L. Younes. Computing deformation metric mappings via geodesic flows of diffeomorphisms. *International Journal of Computer Vision*, 6:139–157, 2005.

[5] L. G. Brown. A survey of image registration technique. *ACM Computing Surveys*, 24:326–376, 1992.

[6] M. Davis, A. Khotanzad, D. Flamig, and S. Harms. Physics-based coordinate transformation for 3-d image matching. *IEEE Transactions on Medical Imaging*, 16:317–328, 1997.

[7] E. Denton, L. Sonoda, D. Rueckert, S. Rankin, C. Hayes, M. Leach, D. Hill, and D. Hawkes. Comparison and evaluation of rigid, affine, and nonrigid registration of breast mr images. *Journal of Computer Assisted Tomography*, 23:800–805, 1999.

[8] F. Dufaux and J. Konrad. Efficient, robust, and fast global motion estimation for video coding. *IEEE Transactions on Image Processing*, 9(3):497–501, Mar. 2000.

[9] J. Fan and I. Gijbels. *Local Polynomial Modeling and Its Applications*. Chapman and Hall, London, 1996.

[10] L. Freire, A. Roche, and J. F. Mangin. What is the best similarity measure for motion correction in fmri time series? *IEEE Transactions on Medical Imaging*, 21:470–484, May 2002.

[11] A. Goshtasby and G. C. Stockman. Point pattern matching using convex hull edges. *IEEE Transactions on Systems, Man and Cybernetics*, 15:631–637, 1985.

[12] P. Hall and P. Qiu. Blind deconvolution and deblurring in image analysis. *Statistica Sinica*, 17:1483–1509, 2007.

[13] B. Horn and B. Schunck. Determining optical flow. *Artificial Intelligence*, 17(1–3):185–204, 1981.

[14] M. Irani and S. Peleg. Motion analysis for image enhancement: Resolution, occlusion and transparency. *Journal of Visual Communication and Image Representation*, 4(4):324–335, Dec. 1993.

[15] Y. Keller, A. Averbuch, and M. Israeli. Pseudopolar-based estimation of large translation, rotations and scalings in images. *IEEE Transactions on Image Processing*, 14(1):12–22, 2005.

[16] A. Klein, J. Andersson, B. Ardekani, and et al. Evaluation of 14 nonlinear deformation algorithms applied to human brain mri registration. *NeuroImage*, 46:786–802, 2009.

[17] D. Lavine, B. Lambird, and L. Kanal. Recognition of spatial point patterns. *Pattern Recognition*, 16:289–295, 1983.

[18] H. Li, B. S. . Manjunath, and S. K. Mitra. A contour-based approach to multisensor image registration. *IEEE Transactions on Image Processing*, 4(3):320–334, Mar. 1995.

[19] L. Liu, T. Jiang, J. Yang, and C. Zhu. Fingerprint registration by maximization of mutual information. *IEEE Transactions on Image Processing*, 15(5):1100–1110, May 2006.

[20] F. Maes, A. Collignon, D. Vandermeulen, G. Marchal, and P. Suetens. Registration by maximazation of mutual information. *IEEE Transactions on Medical Imaging*, 16:187–198, 1997.

[21] J. Modersitzki. *Fair: Flexible Algorithms for Image Registration*. SIAM, Philadelphia, 2009.

[22] C. Nikou, F. Heitz, J.-P. Armspach, I.-J. Namer, and D. Grucker. Registration of mr/mr and mr/spect brain images by fast stochastic optimization of robust voxel similarity measures. *Neuroimage*, 8:30–43, 1998.

[23] W. Pan, K. Qin, and Y. Chen. An adaptable-multilayer fractional fourier transform approach for image registration. *IEEE Transactions on Pattern Analysis and Machine Intelligence*, 31(3):400–412, 2009.

[24] X. Papademetris, A. Jackowski, R. Schultz, L. Staib, and J. Duncan. Integrated intensity and point-feature nonrigid registration. In *Proceedings of the 7th International Conference on Medical Image Computing and Computer-Assisted Intervention*, pages 763–770, Saint-Malo, France, September 2004.

[25] A. Peter and A. Rangarajan. Maximum likelihood wavelet density estimation with applications to image and shape matching. *IEEE Transactions on Image Processing*, 17(4):458–468, 2008.

[26] J. P. W. Pluim, J. B. A. Maintz, and M. A. Viergever. Mutual-information-based registration of medical images: A survey. *IEEE Transactions on Medical Imaging*, 22:986–1004, Aug. 2003.

[27] P. Qiu. *Image Processing and Jump Regression Analysis*. John Wiley & Sons, New York, 2005.

[28] P. Qiu. A nonparametric procedure for blind image deblurring. *Computational Statistics and Data Analysis*, 52:4828–4841, 2008.

[29] P. Qiu and S. Bhandarkar. An edge detection technique using local smoothing and statistical hypothesis testing. *Pattern Recognition Letters*, 17:849–872, 1996.

[30] P. Qiu and T. Nguyen. On image registration in magnetic resonance imaging. In *2008 International Conference on BioMedical Engineering and Informatics*, pages 753–757. IEEE, May 2008.

[31] P. Qiu and B. Yandell. Jump detection in regression surfaces. *Journal of Computational and Graphical Statistics*, 6(3):332–354, 1997.

[32] A. Rajwade, A. Banerjee, and A. Rangarajan. Probability density estimation using isocontours and isosurfaces: Application to information-theoretic image registration. *IEEE Transactions on Pattern Analysis and Machine Intelligence*, 31(3):475–491, 2009.

[33] N. Ritter, R. Owens, J. Cooper, R. Eikelboom, and P. V. Saarloos. Registration of stereo and temporal images of the retina. *IEEE Transactions on Medical Imaging*, 18:404–418, 1999.

[34] N. Saeed. Magnetic resonance image segmentation using pattern recognition, and applied to image registration and quantitation. *NMR in Biomedicine*, 11:157–167, 1998.

[35] J. Sun and P. Qiu. Jump detection in regression surfaces using both first-order and second-order derivatives. *Journal of Computational and Graphical Statistics*, 16(2):289–311, 2007.

[36] R. Szeliski and J. Coughlan. Spline-based image registration. *International Journal of Computer Vision*, 22(3):199–218, 1997.

[37] N. Tustison, B. Avants, and J. Gee. Directly manipulated free-form deformation image registration. *IEEE Transactions on Image Processing*, 18:624–635, 2009.

[38] Y. Wang and L. Staib. Physical model based non-rigid registration incorporating statistical shape information. *Medical Image Analysis*, 4(1):7–20, 2000.

[39] G. Wu, F. Qi, and D. Shen. Learning-based deformable registration of mr brain images. *IEEE Transactions on Medical Imaging*, 25:1145–1157, 2006.

[40] B. Zitova and J. Flusser. Image registration methods: a survey. *Image and Vision Computing*, 21:977–1000, 2003.

Chen Xing received a B.S. degree in chemistry from Nanjing University, China, and an M.S. degree in chemistry from University of Minnesota. Currently, he is a Ph.D. student of the School of Statistics at the University of Minnesota. His current research interests include jump regression analysis, image denoising, image matching and registration, and image segmentation.

Peihua Qiu received a B.S. degree in mathematics and an M.S. degree in statistics from Fudan University, Shanghai, China, an M.S. degree in statistics from University of Georgia, Athens, GA, and a Ph.D. degree in statistics from University of Wisconsin, Madison, WI. From 1996 to 1998, he was with the Biostatistics Center at the Ohio State University, where he worked on biostatistical research and consulting. He was an assistant professor during 1998-2002, an associate professor during 2002-2007, and has been a full professor since 2007, all in the School of Statistics at the University of Minnesota, Minneapolis, MN. He is an elected fellow of the American Statistical Association, an elected fellow of the Institute of Mathematical Statistics, and an elected member of the International Statistical Institute. Currently, he serves as the associate editors of the Journal of the American Statistical Association and Technometrics. His research interests include curve and surface estimation from noisy data, image segmentation, image denoising, image deblurring, image registration, statistical process control, survival analysis, and longitudinal data analysis.